Modeling the Influence of Gas Pressure on Droplet Impact Using a Coupled Gas/liquid Boundary Element Method

Hongbok Park*, Sam S. Yoon†, Richard A. Jepsen** and Stephen D. Heister***

Kwy Words: Droplet impact, Compressed gas, Splashing, Two-phase flow, Bouncing droplet

Abstract

An inviscid axisymmetric model capable of predicting droplet bouncing and the detailed pre-impact motion, influenced by the ambient pressure, has been developed using boundary element method (BEM). Because most droplet impact simulations of previous studies assumed that a droplet was already in contact with the impacting substrate at the simulation start, the previous simulations could not accurately describe the effect of the gas compressed between a falling droplet and the impacting substrate. To properly account for the surrounding gas effect, an effort is made to release a droplet from a certain height. High gas pressures are computationally observed in the region between the droplet and the impact surface at instances just prior to impact. The current simulation shows that the droplet retains its spherical shape when the surface tension energy is dominant over the dissipative energy. When increasing the Weber number, the droplet surface structure is highly deformed due to the appearance of the capillary waves and, consequently, a pyramidal surface structure is formed; this phenomenon was verified with our experiment. Parametric studies using our model include the pre-impact behavior which varies as a function of the Weber number and the surrounding gas pressure.

1. Introduction

Droplet impact phenomena are readily encountered in raindrop impact and in numerous industrial applications as in inkjet printing, painting, spray-wall impact within the IC-engine, and fire suppression sprays. We are particularly interested in the gas pressure effect on splashing because recent research has shown that the gas plays a significant role in causing the splashing.[1-2]

As per well-known classical experiments,[3] a droplet is known to stick to the impacting substrate at a relatively high impact Weber number when the droplet surface tension energy is not high enough to overcome the droplet's dissipative energy.[4] Upon sticking, the droplet spreads radially and forms a toroidal ring at a relatively low Weber number. At an intermediate Weber number, an azimuthal instability develops and forms "fingers" at the rim of the spreading ring. If the Weber number is increased even more, the droplet "splashes" upon contact with the substrate with fingers shedding individual drops.

There are two schools of thought to reason with the fundamental instability of the splashing and the subsequent finger formation. The debate as to which instability (whether or not the Rayleigh-Taylor type buoyancy driven instability or/and the Kelvin-Helmholtz type shear layer driven instability is important) is the primary source for causing the splashing and the finger formation is a subject which needs further scrutiny.

The debate on whether or not the liquid viscosity plays an important role for the finger formation is another branch of thought that complicates the subject. The impacting substrate conditions (i.e., its wettability, roughness, and temperature) also are known to play a prominent role during the droplet impact. All these aforementioned studies of a single droplet impact have

(2006년 4월 10일 접수 ~ 2006년 5월 18일 심사완료)

*ADD
†Corresponding Author, Member, Mech.Eng.Dept., Korea University
E-mail : skyoon@korea.ac.kr
Tel:(02)3290-3376, FAX: (02)926-9290
**Mech.Environment, Sandia National Lab
***School of Aero. & Astro., Purdue University

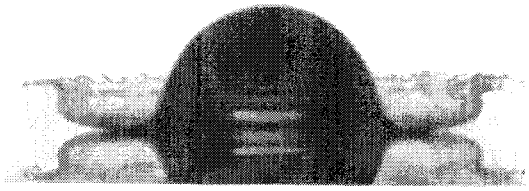

(a) P_{env} = 101 kPa

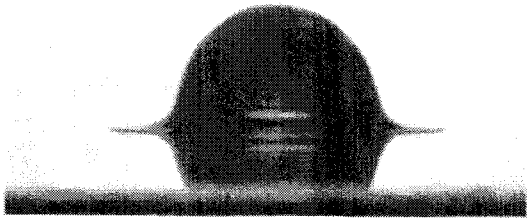

(b) P_{env} = 17 kPa

Fig. 1 Xu et al.'s[6] experiment. When the gas pressure is reduced, splashing is prevented. Reprinted under the permission of Prof. Nagel of University of Chicago

Fig. 2 Development of the vortex rollup motion while gas being compressed due to a falling drop. Photographs are from our ongoing experiment

been used as a basis for the polydisperse spray simulation while Sivakumar and Tropea[5] concluded that the single droplet results should not be extended to the model as a basis for the spray simulation because of the interaction between the multiple droplets, of which results could not be extrapolated using the results of the single droplet impact. While one may be astounded by the magnitude and complexity of the liquid impact physics, one thing is clear: The effect of gas pressure on splashing is conspicuously manifested when the gas pressure varied from 100 kPa to 17 kPa in Fig. 1 of the Xu et al.'s experiment[6] and in the induced vortex rollup motion of gas due to a falling droplet (see Fig. 2 of our current experiment).

We attempt to address this gas pressure effect on the pre-impact condition of a falling droplet using boundary element method (BEM).

The BEM approach is uniquely suited to this problem in that the placement of nodes on the deforming droplet surface maximizes the accuracy in computation of surface curvature, and hence surface tension forces that are known to play a substantial role in the process. Because the experimental results indicate deformation of the impacting droplet is axisymmetric in shape (especially at the pre-impact state), an axisymmetric formulation, is well suited for the application. The model assumes the perfectly smooth impacting substrate and, thus, the effect of the substrate's roughness is neglected. Because of the perfectly smooth substrate assumption, only the bouncing droplet (in which case the surface tension energy is substantially predominant over to the dissipative energy caused by the substrate's roughness) and the pre-impact droplet are considered herein.

2. Modeling

2.1. Two phase flow modeling

Heister[7] provides a complete description of the basic model elements accounting for two-phase flow; only highlights will be presented here in the interest of brevity. An inviscid, incompressible, axisymmetric flow is presumed such that the flow dynamics are governed by Laplace's equation, $\nabla^2\phi = 0$. The boundary element method utilizes an integral representation of this equation to provide a connection between values on the boundary, the local geometry, and the local velocity normal to the boundary, $q = \partial\phi/\partial n$, as follows:

$$\alpha\phi(\vec{r_i}) = \int_S \left[\phi\frac{\partial G}{\partial \hat{n}} - qG\right] ds = 0 \qquad (1)$$

where $\phi(\vec{r}_i)$ is the value of the potential at a point $\vec{r}_i$, S is the boundary of the domain, α is the singular contribution when the integral path passes over the "base point", and G is the free space Green's function corresponding to Laplace's equation. For an axisymmetric domain, the free space Green's function can be expressed in terms of elliptic integrals of the first and second kinds and is a function solely of the instantaneous surface geometry. For this reason, a discrete representation of Eq. (1) can be cast as a linear system of equations relating local ϕ and q values. In the discretization, both ϕ and q are assumed to vary linearly along each element, thereby providing formal second-order accuracy for the method. Since the resulting integrals do not have exact solutions in this case, 4-point Gaussian quadrature is used to maintain high accuracy of integration and preserve second-order accuracy overall.

While this governing equation is a linear, nonlinearity in these free surface problems enter through the boundary condition at the interface. The unsteady Bernoulli equation provides a connection between the local velocity potential and the surface shape at any instant in time. Prior formulations[7-8] have provided a derivation of this result suitable for implementation in a Lagrangian surface tracking environment. The dimensionless form of unsteady Bernoulli equation for the liquid surface is given below with three characteristic parameters; droplet radius (a), the impact speed (U), and the liquid density (ρ_l).

$$\frac{\partial\phi}{\partial t}+\frac{1}{2}(\nabla\phi)^2+P_{gas}+\frac{\kappa}{We}-\frac{Bo}{We}z=0 \qquad (2)$$

where ϕ is the velocity potential, κ is the local surface curvature, the Weber and Bond numbers are defined as $We=\rho_l U^2 a/\sigma$ and $Bo=\rho_l g a^2/\sigma$, respectively where σ is the fluid surface tension. The Eulerian-Lagrangian transformation for nodes on the surface moving with the liquid velocity is:

$$\frac{D(\ )}{Dt}=\frac{\partial(\ )}{\partial t}+\nabla\phi\cdot\nabla(\ ) \qquad (3)$$

where the D/Dt denotes a material or Lagrangian derivative. Using this transformation, the dimensionless Bernoulli equation at the free surface for the liquid becomes:

$$\frac{D\phi}{Dt}=\frac{1}{2}(\nabla\phi)^2-P_g-\frac{\kappa}{We}+\frac{Bo}{We}z \qquad (4)$$

Physically, this Bernoulli equation is a Lagrangian form suitable for fluid elements moving with the local velocity of the free surface. Equation (4) includes the effect of dynamic pressure, local gas-phase pressure, capillary, and hydrostatic pressure contributions, respectively.

An analogous treatment for the gas phase is provided below:

$$\varepsilon\frac{D\phi_g}{Dt}=(\varepsilon\nabla\phi\cdot\nabla\phi_g)-\frac{\varepsilon}{2}(\nabla\phi_g)^2-P_{gas} \qquad (5)$$

where ε is the density ratio between gas and liquid ($\varepsilon=\rho_g/\rho_l$). Mathematically, Eqs. (4) and (5) provide a system of relations to describe the evolution of the free surface. These nonlinear boundary conditions are coupled at the interface between the gas and liquid phases. Since the gas nodes on the interface are set to be coincident with nodes in the liquid phase, the liquid velocity is used to advect both sets of nodes on the interface. The kinematic boundary condition provides the necessary relationships to integrate this motion:

$$\frac{Dz}{Dt}=\frac{\partial\phi}{\partial s}\cos\beta-q\sin\beta,\ \frac{Dr}{Dt}=\frac{\partial\phi}{\partial s}\sin\beta+q\cos\beta \qquad (6)$$

where β is the local slope of the wave with respect to the horizontal direction and r and z are radial and axial coordinates, respectively. Equations (4)-(6) are integrated in time using the 4th-order Runge-Kutta scheme to provide the evolution of the velocity potential and the motion of the free surface. For long integrations or resolution of highly distorted surfaces, points on the free surface will tend to bunch in regions of higher curvature as a result of the free-surface motion. For this reason, the points on the free surface are redistributed at each time step using a cubic spline fitting of the instantaneous shape. Fourth-order accuracy is also employed in computing all surface derivatives in order to maximize accuracy of the surface evolution method. The Laplace equation is solved to update velocities and the process is marched forward in time.

2.2 Computational details

A schematic of the computational domain for two phase flow is shown in Fig. 3. The outer boundary for the gas domain, which is fixed in space, is large enough to encompass the liquid droplet for the entire

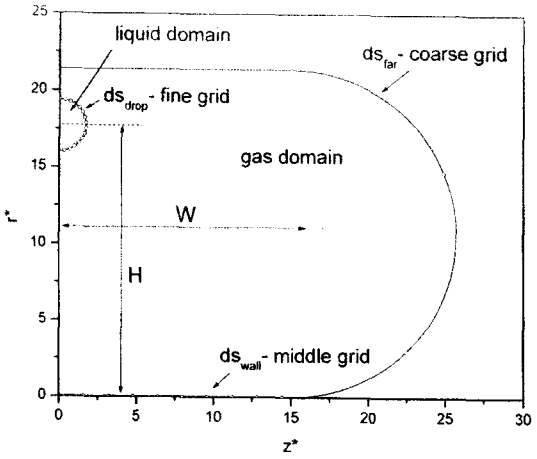

Fig. 3 A schematic for the computational domain of the two phase flow

duration of the calculation. If this outer boundary is placed far enough from the liquid domain, the influence of the outer boundary condition to the flow field around a liquid droplet is negligible. Therefore relatively the coarse grid can be used along this outer boundary. The impacting wall, the bottom wall of this schematic, is considered as a smooth dry wall. This boundary condition can be treated simply as no flux condition through the wall, i.e. q=0. Note here that the dissipative energy induced by the substrate's roughness is not taken into account in the current model. Because the outer boundary is relatively long in length, the computational time is heavily dependent on the grid size of this outer boundary. The high grid resolution applied around the liquid droplet also adds much computational time.

The appropriate initial grid spacing for the inner/outer boundary was found through the grid convergence study. The typical grid spacing for the liquid droplet surface (ds_{drop}) and for the wall boundary (ds_{wall}) with respect to the droplet radius were found to be ds_{drop}=0.02 and ds_{wall}=0.04, respectively. The grid spacing for the outer boundary (ds_{far}) was set as $ds_{far}=5ds_{wall}$. A typical calculation involved about 250 nodes along the liquid droplet and about 400 nodes along the outer boundary.

The following parameters and the fluid properties were set to be consistent with those of the experiment

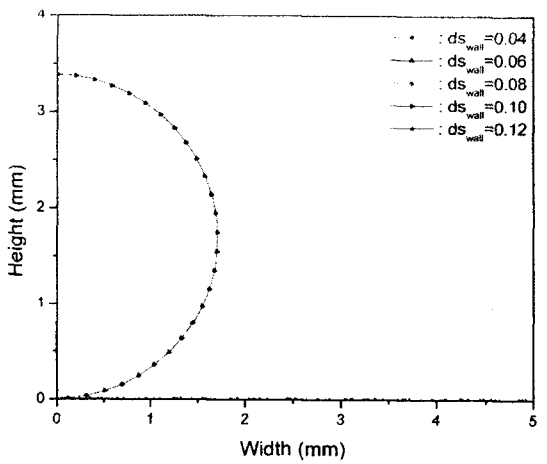

(a)

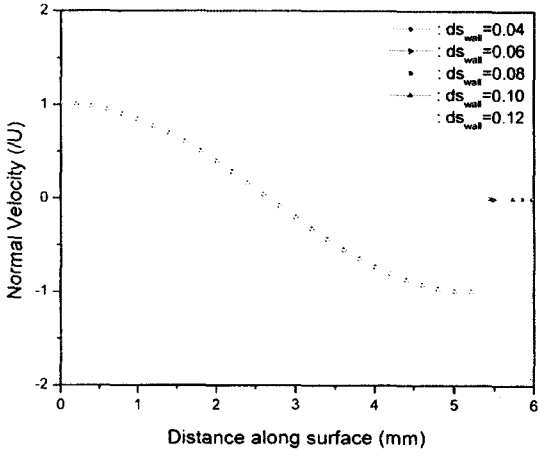

(b)

Fig. 4 Droplet shape and gas normal velocity along the droplet's surface for various ds_{wall}

of Xu et al.[6]: The radius of the alcohol droplet was set as a=1.7 mm. The droplet impact velocity was U = 3.74 m/s. The alcohol density and its surface tension were ρ_l=789 kg/m^3 and σ=0.0224 kg/s^2, respectively. The applied Weber and Bond numbers were, therefore, $We = \rho_l U^2 a/\sigma$=837.9 and $Bo=\rho_l g a^2/\sigma$=0.998, respectively. The density ratio was set as $\varepsilon=\rho_g/\rho_l$=0.00158. The dimensionless environmental gas pressure is defined as $P^*_{env} = P_{atm}/U^2\rho_l$ and, thus, its numerical value is approximately $P^*_{env}\approx 9$ under the given atmospheric pressure, P_{atm}=101 kPa or 1 atm. The liquid droplet is initially located 1 droplet diameter away from the upper outer boundary in our simulation as

indicated in Fig. 3.

The droplet center was initially located at $17a$ height from the bottom substrate's wall with 1 atm. A series of convergence tests for the grid spacing and the integration time were performed. Fig. 4 shows the droplet shapes and the normal velocities with the grid size of the outer boundary at the instance of impact. As shown in Fig. 4, there is a good collapse of data for the various grid sizes applied. These converged results are an indicative of the solution independence from the grid spacing, ds_{wall}. It should be mentioned that the results also were independent from the various widths of gas domain (see the definition of W in Fig. 3). The results are nearly identical that most data overlap together. These converged results allude us to that we may use a coarser grid and smaller gas domain to expedite the computational time. However, it is cautioned that the grid size be small enough to capture the detailed physics at the droplet surface in contact with the substrate. Moreover, one should envision the expansion of the spreading droplet, in which case the fine grid spacing is necessary. To be impervious, we have chosen the large gas domain size and the fine grid spacing as follows: W=15a, H=37a, and ds_{wall}=0.04, where H represents the height measured from the initial location of the droplet to the bottom substrate. A typical calculation takes about 5 days on 1-*GHz* CPU machine.

3. Results and discussions

3.1 Droplet bouncing in vacuum

In Fig. 5, a typical bouncing droplet is simulated and compared with the experimental image. In Fig. 6, the "doughnut-shaped" droplet with an erupting jet at the center is simulated and compared with the experimental image. This jet eruption is produced because of the cavity formed at the droplet's top center during the surface deformation and the subsequent wave traveling during the impact. This wave traveling is further manifested in our own experimental images in Fig. 7. As shown, the capillary waves travels along the droplet's surface and the wave amplitude reduces its size and, eventually, disappears at the droplet's top.

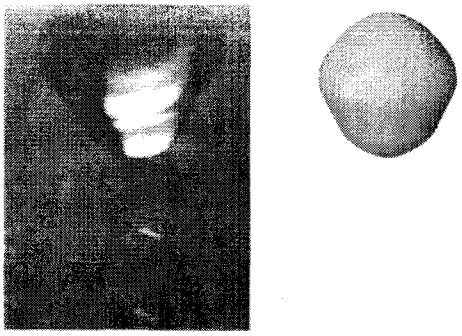

(a) (b)

Fig. 5 Typical rebounding droplets. (a) Experimental image by Renardy et al.[9] is reprinted under the permission of Journal of Fluid Mechanics (b) Model prediction

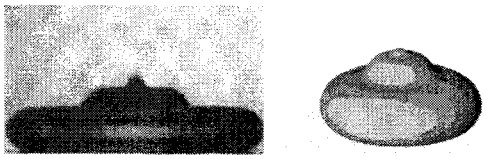

(a) (b)

Fig. 6 Appearance of the pyramidal surface structure when $We\,Ca < 1$. (a) Experiment image by Renardy et al.[9] is reprinted under the permission of Journal of Fluid Mechanics (b) Modeling prediction

3.2 Effect of gas presence

The effect of the environmental gas was investigated in the Xu et al.'s[6] experimental condition, where the size of an alcohol droplet was 1.7 mm in radius and its impact velocity was 3.74 m/sec. In this Section 3.2, we attempt to show, computationally, the effect of gas presence, which was compellingly evidenced by Xu et al.[6] experimentally.

The droplet shape and its pressure distribution along its surface at the instance of impact at 1 atm gas pressure are shown in Fig. 8. Note here that the droplet is released from far upstream location, rather than assuming that the droplet is already in contact with the impacting substrate at t=0. Thus the gas pressure variations beneath the droplet are properly taken into account. It is observed in Fig. 8(a) that our model predicts the slight deformation of the falling droplet just prior to the impact. In Fig. 8(b), the increase in the gas pressure along the droplet surface is shown. Note that

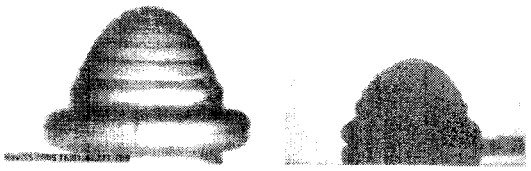

(a) Water droplet (b) Balloon containing water

Fig. 7 Typical pyramidal shape of droplets formed on plexiglas. Photographs are from our ongoing

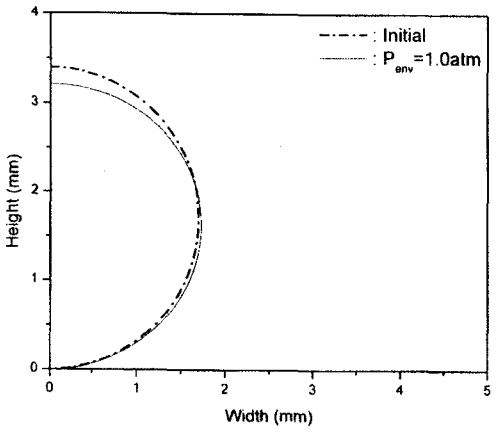

(a)

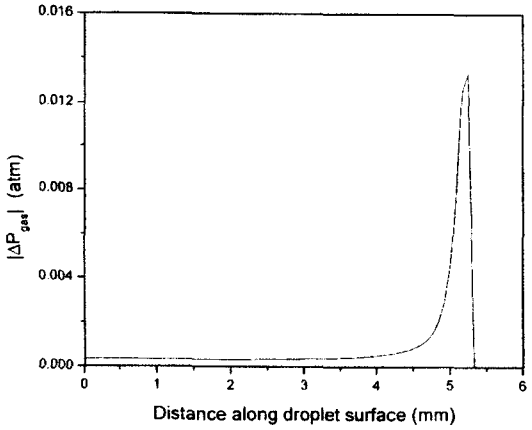

(b)

Fig. 8 The ambient pressure effect on (a) the droplet shape and (b) the pressure distribution along the droplet surface during impact

the x-axis represents the length of the semi-perimeter of the droplet circle so that s = 0 represents the droplet's top while $s=\pi a \approx 5.34\ mm$ represents the droplet's bottom in contact with the substrate. As shown, the gas pressure peaks at around $|\Delta P_{gas}| = |P_{gas} - P_{env}| \approx 0.013$

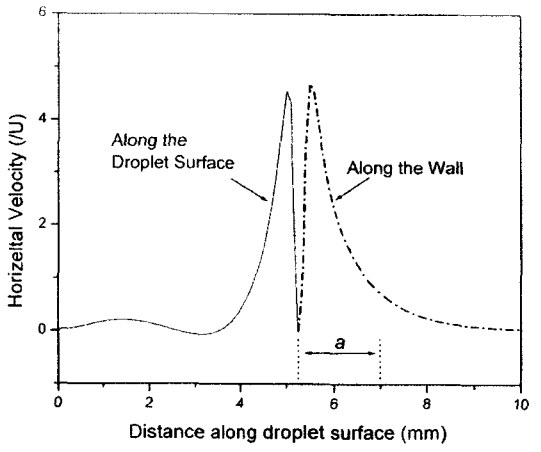

(a)

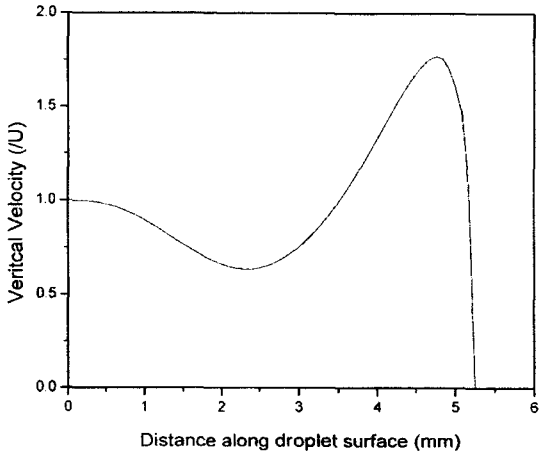

(b)

Fig. 9 The (a) horizontal and (b) vertical gas velocity profiles along the droplet surface of a falling droplet at the instance of impact under an ambient pressure condition

atm, P_{env}=1 where atm and, thus, the moderate increase of the gas pressure due to the falling droplet lies with ~1.3%.

As for the gas velocity in Fig. 9, the maximum horizontal velocity (~ 4.5U m/s) is larger than the vertical velocity (~ 1.75U m/s). This result is in good agreement with the experimental observation of Refs[1-2].

The gas was accelerated because of its volume was squeezed between the droplet falling against the substrate. In this case, the droplet surface is susceptible to the Kelvin-Helmholtz instability, which may be the fundamental cause for splashing. In Fig. 9(a), the gas near the substrate is also escaping with nearly the same

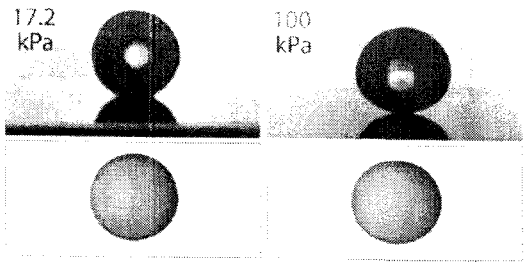

Fig. 10 The droplet shape comparison of a falling droplet at the instance of impact between the case (a) in nearly vacuum condition and (b) in P_{env}=1 atm pressure condition. Experimental images are re-printed under the permission of Prof. Nagel of University of Chicago

velocity as the velocity along the droplet's surface. The high peak region is located near the collapsed region within the droplet's radius, as noted with the symbol "*a*" in Fig. 9(a). It is noteworthy that the gas velocity profile is nearly symmetrical at the contact point because the droplet surface at the point is flat and its tangent is parallel to the substrate's wall. However the symmetry disappears while being farther away from the contact point as shown in Fig. 9(a). This appearance of the asymmetry is because the droplet surface's tangent is no longer in parallel to the substrate's wall. In Fig. 9(b), the vertical gas velocity also reaches its maximum value (~1.75U m/s) near the droplet's bottom. This vertical component of the gas velocity is responsible for the momentum of the crown-shaped "corona" of splashing such as in Fig. 1(a). Thus, this vertical component is essential for inducing corona splashing.

Fig. 10 compares the droplet at 100 kPa ambient pressure with the slightly deformed droplets at nearly vacuum conditions, 17.2 kPa. The slight deformation of the droplet due to the gas pressure is obvious in the experimental images. While the computational results are a bit difficult to see the qualitative difference in shape, the quantitative difference is shown and discussed in the following figures.

3.3. Weber number effect

Fig. 11 shows the deformed droplet and its pressure distribution along droplet's surface at the various Weber numbers. When the Weber number is relatively low (i.e., $We=We_0/100$, where We_0=837.9), nearly no deformation of the droplet is observed as its data (see the "▲" symbol) are overlapped with those of the initial shape (see the dotted line in Fig. 11(a). When the Weber number is relatively high (i.e., $We=100We_0$), the droplet is deformed in a similar manner as in the case of $We=We_0$. These similar results indicate that the droplet's shape is independent from the Weber number when the Weber number exceeds a certain critical value.

One may envision increasing the Weber number while increasing the impact speed (i.e., $We \propto U^2$) under the fixed values of droplet diameter and liquid properties. However, this dynamic pressure term does

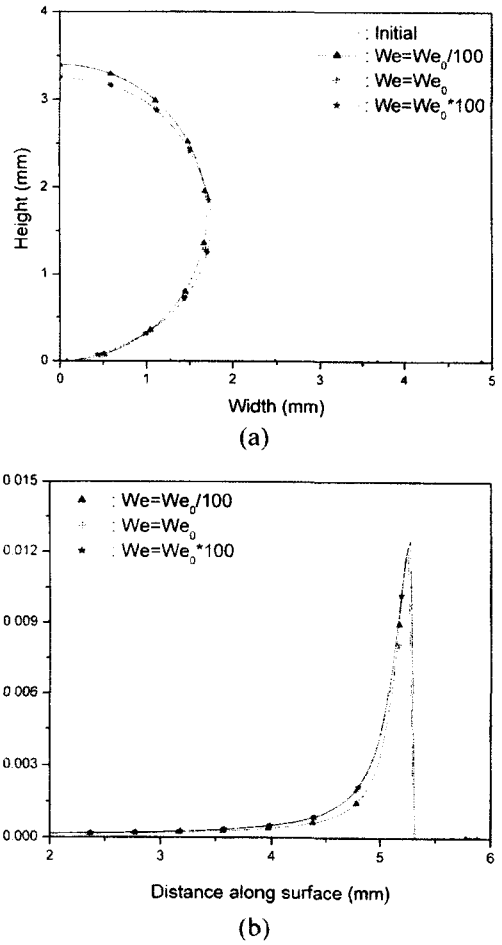

Fig. 11 The Weber number effect on (a) the droplet shape and (b) the pressure distribution along the droplet surface

not contribute much to the total pressure (or stagnation pressure) at the bottom contact point of the falling droplet. For example, the total (or stagnation) pressure is $P_{env}+\rho_g U^2/2$ for an incompressible flow. While P_{env} = 101 kPa, it is difficult to produce the dynamic pressure comparable to the static pressure unless the droplet were traveling at supersonic speed. For this reason, the droplet deformation was not observed with the moderate change in the Weber number as shown in Fig. 11(a). This result is consistent with the physical explanation mentioned above.

3.4. Pressure effect

Fig. 12 shows the droplet deformation and the gas pressure distribution along the droplet surface at various P_{env}. As shown in Fig. 12(a), the droplet deforms with greater curvature with larger value of P_{env}, of which pattern is expected. We have computationally shown that the gas pressure is indeed important in inducing the droplet deformation and, eventually, affects for the droplet to splash. This linear pattern of the increase in $|\Delta P_{gas}|$ is also interesting as its peak values reaches approximately 0.013 atm and 0.025 atm at P_{env}=1 atm and 2 atm, respectively. This pattern indicates that the 1 atm increase in the ambient (or environmental) pressure results in about 1.3% increase in the stagnation gas pressure at the bottom contact point of the falling droplet. Using this linear relation, the peak value of the stagnation pressure at given P_{env}=3 atm would be approximately ~ 0.04 atm and would be ~ 0.13 atm if P_{env}=10 atm.

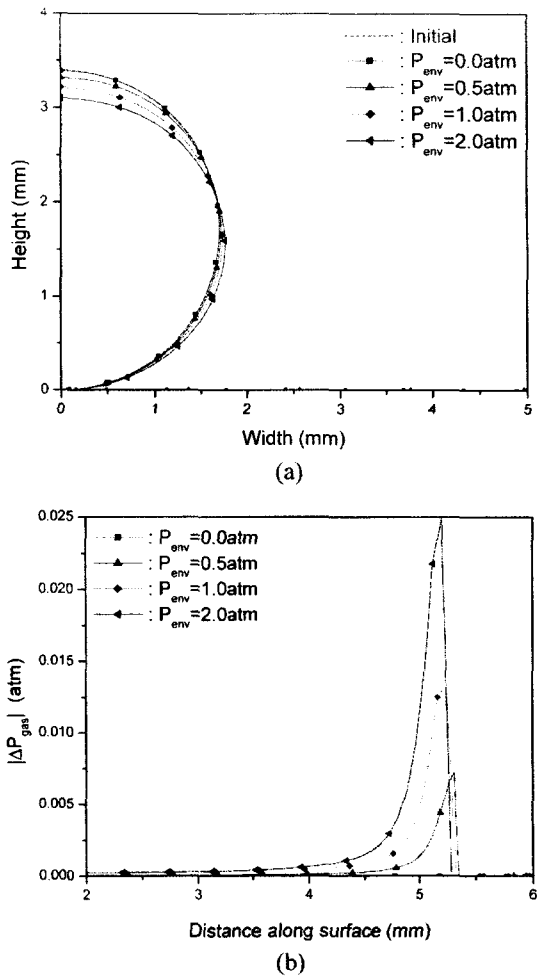

Fig. 12 The ambient gas pressure effect on (a) the droplet shape and (b) the pressure distribution along the droplet surface

4. Conclusions

The effect of gas pressure on the droplet deformation has been studied computationally. The numerical accuracy was first verified through the grid convergence studies and the results were qualitatively compared to our ongoing experimental results as well as other authors' experiment. Moreover, the droplet bouncing was simulated for the case where the Weber number was relatively low that the surface tension energy dominates over the dissipative energy of friction. The capillary surface waves appeared during the simulation, which also was observed in the experiment. The high escaping gas velocity, accelerated by the compression between the falling droplet and the stationary substrate wall, was observed. The maximum value of the escaping gas velocity reached nearly 5 times the impact speed, whose result was consistent with our experimental observation. It was also found that the peak stagnation gas pressure at the droplet's bottom at the time of impact has a linear relationship with the increase of the ambient pressure; the 1 atm environmental (or ambient) pressure will induce 1.3% increase in the stagnation gas pressure at the contact point.

Acknowledgements

The authors gratefully acknowledge the support of the Sandia National Laboratories (SNL) under Grant No. LDRD05-0030. SNL is a multiprogram laboratory operated by Sandia Corporation, a Lockheed Martin Company for the United States Department of Energy's National Nuclear Security Administration under contract DE-AC04-94AL85000.

References

(1) R. A. Jepsen, S. S. Yoon, B. Demosthenous, "Effects of air on splashing during a large droplet impact", Atomization and Sprays, accepted, 2006.

(2) S. S. Yoon, R. A. Jepsen, M. R. Nissen, "Hern, O., "Experimental investigation on splashing and nonlinear fingerlike instability of large water drops, Physics of Fluids," submitted, 2006.

(3) A. M. Worthington, A Study of Splashes Longmans & Green, London, 1908.

(4) S. D. Aziz, S. Chandra, "Impact, recoil and splashing of molten metal droplets", Int. J. Heat Mass Transfer, 20, Vol. 43, 2000, pp. 2841-2857.

(5) D. Sivakumar, C. Tropea, "Splashing impact of a spray onto a liquid film, Physics of Fluids", Vol. 14, 2002, L85-L88.

(6) L. Xu, W. Zhang, S.R. Nagel, "Drop splashing on a dry smooth surface", Physical Review Letter, Vol. 94, No. 184505, 2005

(7) S. D. Heister. "Boundary element methods for two-fluid free surface flows", Engineering Analysis with Boundary Elements, Vol. 19, 1997, pp. 309-317.

(8) C. A. Spangler, J. H. Hilbing, and S. D. Heister. "Nonlinear modeling of jet atomization in the wind-induced regime", Physics of Fluids, 1995;Vol. 7, 1995, pp. 964.

(9) Y. Renardy, S. Popinet, L. Duchemin, M. Renardy, S. Zaleski, C. Josserand, M.A. Drumright-Clarke, D. Richard, C. Clanet, D. Quere, "Pyramidal and toroidal water drops after impact on a solid surface", J. Fluid Mech., Vol. 484, 2003, pp. 69-83.